Femtoscopic study of coupled-channels $N\Xi$ and $\Lambda\Lambda$ interactions

Y. Kamiya,[1,2] K. Sasaki,[3] T. Fukui,[4] T. Hyodo,[5,2] K. Morita,[6,4] K. Ogata,[7,8,9] A. Ohnishi,[10] and T. Hatsuda[2]

[1]*CAS Key Laboratory of Theoretical Physics, Institute of Theoretical Physics, Chinese Academy of Sciences, Beijing 100190, China*
[2]*RIKEN Interdisciplinary Theoretical and Mathematical Science Program (iTHEMS), Wako 351-0198, Japan*
[3]*Division of Scientific Information and Public Policy, Center for Infectious Disease Education and Research (CiDER), Osaka University, Suita 565-0871, Japan*
[4]*RIKEN Nishina Center, Wako 351-0198, Japan*
[5]*Department of Physics, Tokyo Metropolitan University, Hachioji 192-0397, Japan*
[6]*National Institutes for Quantum Science and Technology, Rokkasho Fusion Institute, Rokkasho 039-3212, Japan*
[7]*Research Center for Nuclear Physics, Osaka University, Ibaraki 567-0047, Japan*
[8]*Department of Physics, Osaka City University, Osaka 558-8585, Japan*
[9]*Nambu Yoichiro Institute of Theoretical and Experimental Physics, Osaka City University, Osaka 558-8585, Japan*
[10]*Yukawa Institute for Theoretical Physics, Kyoto University, Kyoto 606-8502, Japan*

(Received 1 September 2021; revised 13 November 2021; accepted 11 January 2022; published 28 January 2022)

The momentum correlation functions of $S = -2$ baryon pairs ($p\Xi^-$ and $\Lambda\Lambda$) produced in high-energy pp and pA collisions are investigated on the basis of the coupled-channels formalism. The strong interaction is described by the coupled-channels HAL QCD potential obtained by lattice QCD simulations near physical quark masses, while the hadronic source function is taken to be a static Gaussian form. The coupled-channels effect, the threshold difference, the realistic strong interaction, and the Coulomb interaction are fully taken into account for the first time in the femtoscopic analysis of baryon-baryon correlations. The characteristic features of the experimental data for the $p\Xi^-$ and $\Lambda\Lambda$ pairs at the Large Hadron Collider are reproduced quantitatively with a suitable choice of nonfemtoscopic parameters and the source size. The agreement between theory and experiment indicates that the $N\Xi$ ($\Lambda\Lambda$) interaction is moderately (weakly) attractive without having a quasibound (bound) state.

DOI: 10.1103/PhysRevC.105.014915

I. INTRODUCTION

Dibaryons in the strangeness $S = -2$ sector have long attracted theoretical and experimental attention [1–3]. Among others, the Pauli blocking among valence quarks does not operate and the color-spin interaction is attractive for the $H(uuddss)$ dibaryon with $(I, J^\pi) = (0, 0^+)$, and then it was suggested to be a possible deeply bound state below the $\Lambda\Lambda$ threshold in the flavor SU(3) limit [4]. While the discovery of the double Λ hypernuclei [5,6] ruled out the deeply bound H, the existence and the mass of the H are still under debate in connection with the interactions of the $S = -2$ baryon-baryon pairs, $\Lambda\Lambda$ and $N\Xi$, which couple with the H dibaryon. Because the baryon-baryon interactions are the basic inputs to construct the equation of state of baryonic matter, such studies are also crucial for identifying the role of Λ and Ξ^- in neutron star matter at several times the nuclear matter density in relation to the so-called hyperon puzzle in neutron star structure originally pointed out in Ref. [7], as well as to the observed constraints on mass and radius of neutron stars [8]. We need precise knowledge on the two-body interactions in the strangeness sector at finite and zero densities to improve the theoretical predictions.

As for the existence of the H dibaryon, there are three possibilities: the H exists as a loosely bound state below the $\Lambda\Lambda$ threshold, as a quasibound state between the $\Lambda\Lambda$ and $N\Xi$ thresholds, or neither a bound nor a quasibound state exists as shown in Fig. 1. Weak decay was observed for the double hypernucleus ${}^{\ 6}_{\Lambda\Lambda}\mathrm{He}$, where the binding energy of 2Λ particles is $B_{\Lambda\Lambda}({}^{\ 6}_{\Lambda\Lambda}\mathrm{He}) = 6.91$ MeV. If the bound H with mass $M_H < 2M_\Lambda - B_{\Lambda\Lambda}({}^{\ 6}_{\Lambda\Lambda}\mathrm{He})$ exists, ${}^{\ 6}_{\Lambda\Lambda}\mathrm{He}$ needs to decay strongly by emitting H. Thus the mass region of a bound H state is limited to $2M_\Lambda - B_{\Lambda\Lambda}({}^{\ 6}_{\Lambda\Lambda}\mathrm{He}) < M_H < 2M_\Lambda$. Also, recent femtoscopic studies of the $\Lambda\Lambda$ correlation functions favor the attractive scattering length, and therefore disfavor the existence of a bound state below the $\Lambda\Lambda$ threshold [9–11]. Moreover, the latest $(2 + 1)$-flavor lattice QCD simulations close to the physical point indicate that there is no bound state below $\Lambda\Lambda$ [12].

Hence the current interest in the $S = -2$ dibaryons is shifted to the higher energy region around the $N\Xi$ threshold in the same isospin-spin $(I, J^\pi) = (0, 0^+)$ channel, which

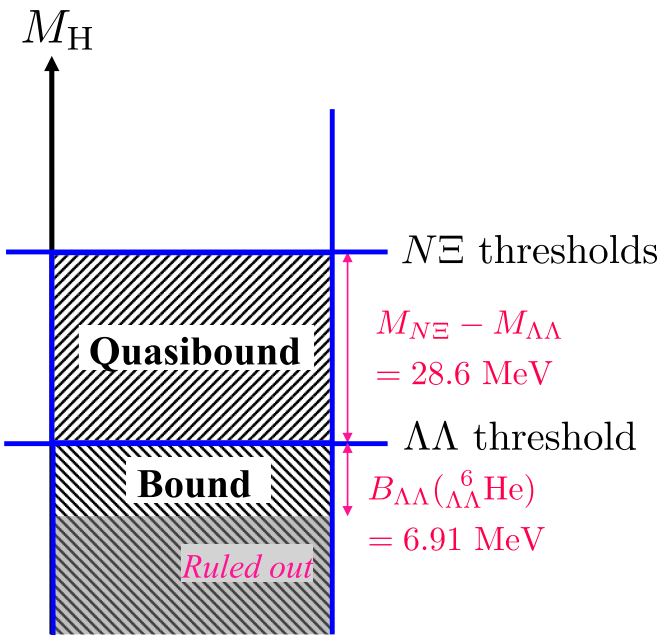

FIG. 1. Categories of the H dibaryon mass region. The bound H region is defined as $M_H < 2M_\Lambda$. The "quasibound" state is defined as a physical state between the $\Lambda\Lambda$ and $N\Xi$ thresholds, and it is a bound state of $N\Xi$ and a resonance state of $\Lambda\Lambda$. For a quasibound state, the eigenmomenta q in $N\Xi$ channels need to have positive imaginary parts, so that the asymptotic wave function $\propto \exp(iqr)/r$ converges to zero. The imaginary part of the eigenmomentum in the $\Lambda\Lambda$ channel needs to be negative, and the resonance wave function diverges asymptotically. If these eigenmomentum conditions are not satisfied for a pole, that pole does not represent a physical state and is called a virtual pole. See Appendix B for details.

couples to $\Lambda\Lambda$ (see Fig. 1). The $N\Xi$ interaction is considered to be moderately attractive as indicated by the existence of the Ξ hypernucleus ${}^{15}_{\Xi}$C [13–15], by femtoscopic studies of the $N\Xi$ interaction [16,17], by chiral effective field theory calculations [18,19], and by lattice QCD simulation [12]. This attractive interaction may drive a quasibound state between the $\Lambda\Lambda$ and $N\Xi$ thresholds or a resonance above the $N\Xi$ thresholds. Therefore, it is of great importance to make a quantitative comparison between theoretical analysis and the experimental data with the $N\Xi$-$\Lambda\Lambda$ coupled-channels framework and the state-of-the-art baryon-baryon interactions (e.g., [20,21]).

It has been known that the correlation function in high-energy collisions is sensitive to the interaction when the absolute value of the scattering length (a_0) is comparable to or larger than the emission source size R of hadronic pairs, where $R \simeq$ 1–5 fm depending on the reactions (pp, pA, or AA) [9,22–28]. It has been also argued that the source size dependence of the correlation function is useful to deduce the existence or nonexistence of hadronic bound states [27,28].

In the present paper, we focus on the momentum correlations of $N\Xi$ and $\Lambda\Lambda$ in pp and pA collisions. Recent experimental measurements of such correlations have opened a new way to probe the hyperon interactions which are not accessible in the standard scattering experiments [29]. Theoretically, the correlation function can be described by the convolution of the source function and the relative wave function in the pair rest frame [30–34].

We consider the coupled-channels formalism ($p\Xi^-$-$n\Xi^0$-$\Lambda\Lambda$ for $J = 0$ and $p\Xi^-$-$n\Xi^0$ for $J = 1$) with the latest HAL QCD coupled-channels potential in the s-wave obtained from the $(2 + 1)$-flavor lattice QCD simulations at almost physical quark masses [12]. The threshold differences and the Coulomb interaction are taken into account simultaneously. For the source function in pp and pA reactions, we take a static and spherically symmetric Gaussian form with a source size R. Our theoretical calculations are then compared with the experimental data of $p\Xi^-$ and $\Lambda\Lambda$ correlation functions in pp and pA collisions at the Large Hadron Collider (LHC) [10,11,16,17]. Similar analysis with all ingredients (coupled channels, threshold difference, realistic strong interaction, and Coulomb interaction) was recently performed for the $S = -1$ meson-baryon system ($\bar{K}N$-$\pi\Sigma$-$\pi\Lambda$) for the first time [28].

This article is organized as follows. In Sec. II, we briefly review the $S = -2$ baryon-baryon potential from lattice QCD calculations. In Sec. III, the theoretical framework to calculate the $p\Xi^-$ and $\Lambda\Lambda$ correlation functions in the coupled-channels framework is discussed in detail. In Sec. IV, we show the determination of the phenomenological parameters from the experimental data at LHC on the basis of the formalism in the previous section. In Sec. V, our theoretical results of $p\Xi^-$ and $\Lambda\Lambda$ correlation functions and the experimental data are compared. Section VI is devoted to a summary and concluding remarks. The low energy scattering parameters from a modified HAL QCD potential, the location of the virtual pole near the $N\Xi$ threshold, and an analytic model of the correlation function with Gamow factor are discussed in Appendices A–C, respectively.

II. $S = -2$ COUPLED-CHANNELS POTENTIAL FROM LATTICE QCD

Throughout this paper, we employ the state-of-the-art coupled-channels $N\Xi$-$\Lambda\Lambda$ potential below the $\Sigma\Sigma$ threshold obtained by $(2 + 1)$-flavor lattice QCD simulations near the physical point ($m_\pi = 146$ MeV and $m_K = 525$ MeV) [12]. It is the local and energy-independent potential in the leading-order of the derivative expansion at low energies [35,36]. The coupled-channels $N\Xi$-$\Lambda\Lambda$ potential is fitted in terms of a combination of Gaussian, Yukawa, and squared-Yukawa functions with the pion and kaon masses on the lattice mentioned above [12]. Shown in Fig. 2 are the results of the fitted potentials in the isospin-spin basis with the notation ${}^{2I+1,2s+1}L_J$ with the isospin I and the spin s. The statistical error of the potentials originating from the Monte Carlo simulations is evaluated by the standard jackknife method and is denoted by the colored shadows, while the systematic error originating from the truncation of the derivative expansion is estimated by the t dependence of the potentials, with t being the temporal distance between source and sink operators in the lattice unit [12]. The important features of the HAL QCD potential are (i) a large attraction in the $I = s = 0$ $N\Xi$ channel (the upper

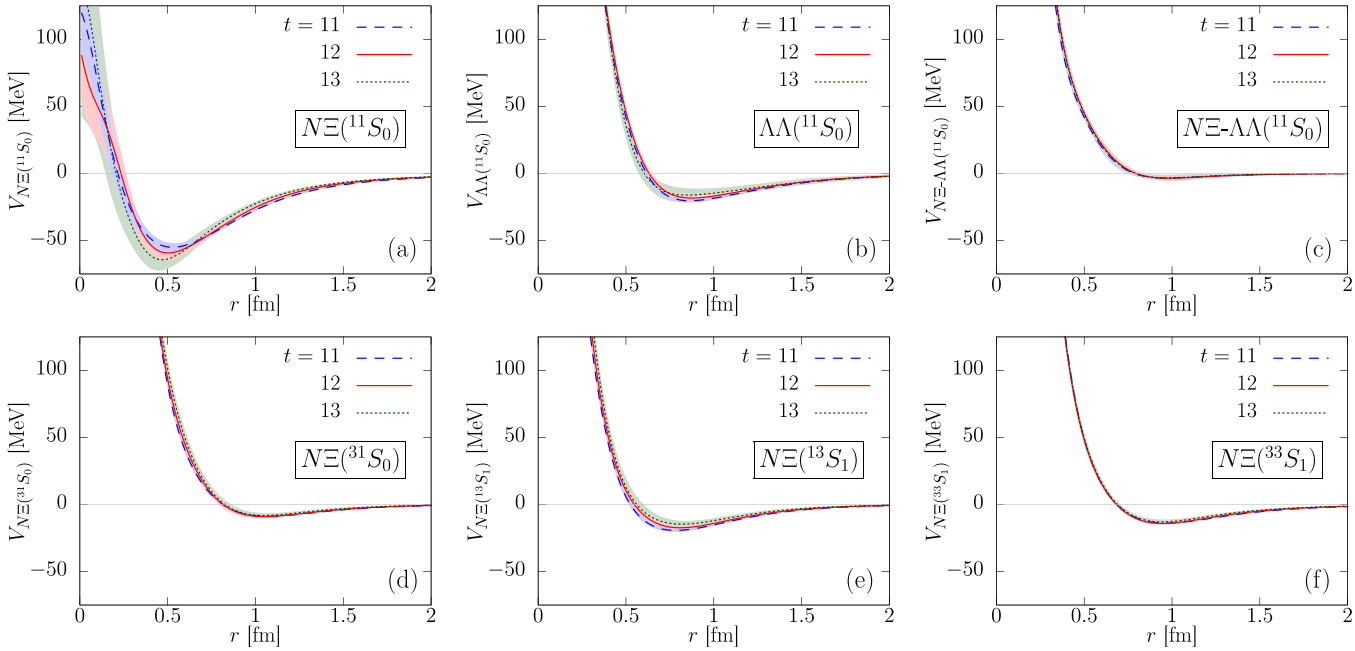

FIG. 2. The s-wave coupled-channels HAL QCD potential for three temporal distances, $t = 11$, 12, and 13 at almost physical quark masses [12]. The colored shadow denotes the statistical error of each potential.

left panel), (ii) a weak mixing between $N\Xi$ and $\Lambda\Lambda$ (the upper right panel) at low energy, and (iii) a weak attraction in the $\Lambda\Lambda$ channel (the upper middle panel).

As low energy constants characterizing the strong interaction, we calculate the scattering length a_0 and the effective range $r_{\rm eff}$ in the s-wave by solving the Schrödinger equation with the HAL QCD potential in Fig. 2 without the Coulomb interaction. Here we take the nuclear and atomic physics convention, where the s-wave phase shift at low energies is given by

$$q \cot \delta_0(q) = -\frac{1}{a_0} + \frac{1}{2} r_{\rm eff} q^2 + \cdots , \tag{1}$$

with q being the relative momentum. Table I summarizes the results where the central values of a_0 and $r_{\rm eff}$ are obtained from $t = 12$ with the statistical errors evaluated by the jackknife method and the systematic errors estimated from $t = 11$ and 13. Unlike the procedure in Ref. [12] where baryon masses measured on the lattice are used in the kinetic part of the Schrödinger equation, we use the experimental baryon masses of p, n, Λ, Ξ^-, and Ξ^0.[1]

Note that a_0 in $\Lambda\Lambda(J = 0)$ and $n\Xi^0(J = 1)$ channels in Table I are strictly real since there are no two-baryon states below, while those in $p\Xi^-(J = 0)$ and $n\Xi^0(J = 0)$ channels are complex due to the coupling to the lower $\Lambda\Lambda$ channel. Also, a_0 in the $p\Xi^-(J = 1)$ channel is complex in principle due to the coupling to the lower $n\Xi^0(J = 1)$ channel.

Solving the Schrödinger equation, we find that neither bound H dibaryon below the $\Lambda\Lambda$ threshold nor a quasibound state below the $N\Xi$ threshold are allowed with the HAL QCD potential, although the interactions in both channels are attractive. Also, the large $|a_0|$ in the $n\Xi^0(J = 0)$ channel indicates that this system is close to the unitary regime. In fact, there appears a virtual pole in the complex energy plane (see Appendix B). The imaginary part of a_0 in the $p\Xi^-$ $(J = 1)$ channel is essentially zero, which implies that the transition between $p\Xi^-$ to $n\Xi^0$ is very weak: This is partly due to the fact that the $N\Xi$ potential in $I = 0$ (the lower middle panel of Fig. 2) and that in $I = 1$ (the lower right panel of Fig. 2) are very close to each other.

III. COUPLED-CHANNELS CORRELATION FUNCTION WITH COULOMB INTERACTION

In high-multiplicity events of pp and pA collisions as well as in high-energy AA collisions, the hadron production yields are well described by the statistical model, which implies that the hadrons are produced independently. In such a situation, the momentum correlations between outgoing particles are generated by the quantum statistics and the final state interactions. Consider two particles, a and b, with relative momentum $\boldsymbol{q} = (m_b \boldsymbol{p}_a - m_a \boldsymbol{p}_b)/(m_a + m_b)$ observed in the final state. Let this two-particle state be fed by a set of coupled channels, each denoted by j. In the pair rest frame of the two measured particles, their correlation function $C(\boldsymbol{q})$ is given by [34]

$$C(\boldsymbol{q}) = \int d^3 r \sum_j \omega_j S_j(\boldsymbol{r}) |\Psi_j^{(-)}(\boldsymbol{q}; \boldsymbol{r})|^2, \tag{2}$$

[1] In Appendix A, we show the results of a_0 and $r_{\rm eff}$ with the experimental baryon masses in the kinetic term and a modified HAL QCD potential in which $m_{\pi,K}$ in the fitted potential are replaced by the isospin-averaged experimental values of the pion and kaon masses. The results in this procedure are consistent with those of Table I within statistical and systematic errors.

TABLE I. The scattering length (a_0) and the effective range ($r_{\rm eff}$) defined in Eq. (1) in the $p\Xi^-$, $n\Xi^0$, and $\Lambda\Lambda$ channels calculated by using the HAL QCD potential. The Coulomb interaction is switched off. Note that we use the nuclear physics convention for a_0 where the positive (negative) real part corresponds to the repulsive or strongly attractive (weakly attractive) interaction. The statistical and systematic errors are shown in the first and second parentheses, respectively.

Total spin	Baryon pair	a_0 (fm)	$r_{\rm eff}$ (fm)
$J=0$	$p\Xi^-$	$-1.22(0.13)(^{+0.08}_{-0.00}) - i1.57(0.35)(^{+0.18}_{-0.23})$	$3.7(0.3)(^{+0.1}_{-0.1}) - i2.7(0.2)(^{+0.1}_{-0.3})$
	$n\Xi^0$	$-2.07(0.39)(^{+0.28}_{-0.35}) - i0.14(0.08)(^{+0.00}_{-0.01})$	$1.5(0.3)(^{+0.0}_{-0.0}) - i0.2(0.0)(^{+0.0}_{-0.1})$
	$\Lambda\Lambda$	$-0.78(0.22)(^{+0.00}_{-0.13})$	$5.4(0.8)(^{+0.1}_{-0.5})$
$J=1$	$p\Xi^-$	$-0.35(0.06)(^{+0.09}_{-0.07}) - i0.00$	$8.3(1.0)(^{+2.8}_{-1.2}) + i0.0(0.1)(^{+0.1}_{-0.0})$
	$n\Xi^0$	$-0.35(0.06)(^{+0.09}_{-0.07})$	$8.4(1.0)(^{+2.7}_{-1.2})$

where the wave function $\Psi_j^{(-)}$ in the jth channel is written as a function of the relative coordinate $\boldsymbol{r}$ in that channel, with outgoing boundary condition on the measured channel. $S_j(\boldsymbol{r})$ and ω_j are the normalized source function and its weight in the jth channel, respectively: $\int d^3r S_j(\boldsymbol{r}) = 1$ and $\omega_1 = 1$, where we label the measured channel as channel 1. The latter normalization of the source weight follows from the fact that the correlation function must be unity for any momentum q in the noninteracting limit $V_{ij} \to 0$ [34]. In this study, we use the static Gaussian $S_R(r) \equiv \exp(-r^2/4R^2)/(4\pi R^2)^{3/2}$ with source size R for the hadron source function. In this case, the correlation function only depends on $q = |\boldsymbol{q}|$. Thus the correlation function contains information on both the hadron source and the hadron-hadron interactions. We call Eq. (2) the Koonin-Pratt-Lednicky-Lyuboshits-Lyuboshits (KPLLL) formula after the series of works [30–34].

There are essentially four theoretical ingredients to fully utilize the KPLLL formula and to compare with the experimental data: (i) the coupled-channels wave functions, (ii) threshold differences, (iii) the modern hadron-hadron interactions, and (iv) the Coulomb interaction. A comprehensive analysis with all these ingredients was recently carried out for the first time in the case of the K^-p correlation function in high-energy nuclear collisions on the basis of the $\bar{K}N$-$\pi\Sigma$-$\pi\Lambda$ coupled-channels framework [28]. In the subsections below, we generalize this approach applicable to the $N\Xi$-$\Lambda\Lambda$ system.

A. Coupled-channels formalism

Let us first illustrate some features of the coupled-channels wave function for nonidentical particles. We focus on the small momentum region and assume that the strong interaction modifies only the s-wave part of the wave function. The coupled-channels wave function $\Psi_j^{(-)}$ with the outgoing boundary condition can be written as

$$\Psi_j^{(-)}(\boldsymbol{q};\boldsymbol{r}) = (\phi(\boldsymbol{q};\boldsymbol{r}) - \phi_0(qr))\delta_{1j} + \psi_j^{(-)}(q;r), \qquad (3)$$

where $r = |\boldsymbol{r}|$, $\phi(\boldsymbol{q};\boldsymbol{r})$ is the wave function without the strong interaction, $\phi_0(qr)$ is its s-wave component, and $\psi_j^{(-)}(q;r)$ is the total wave function in the s wave affected by the strong interaction.

The wave function $\psi_j^{(-)}(q;r)$ in Eq. (3) can be obtained by solving the coupled-channels Schrödinger equation,

$$\sum_j \left(-\frac{\nabla^2}{2\mu_i}\delta_{ij} + V_{ij}(r) \right) \psi_j(q;r) = E_i \psi_i(q;r), \qquad (4)$$

where $E_i = E - \Delta_i$ with μ_i and Δ_i representing the reduced mass in channel i and the threshold energy difference between channel i and channel 1, respectively. Since $\Delta_1 = 0$, we have $E = E_1$ and $q \equiv \sqrt{2\mu_1 E} = q_1$. Note that $E_{i>1}$ can be positive or negative depending on the scattering energy, while $E \geqslant 0$ for physical scattering.

Unlike the case of the standard scattering problem where the flux of the incoming wave is normalized, the outgoing wave in the measured channel needs to be normalized in the present case under the boundary condition:

$$\psi_j^{(-)}(q;r) \xrightarrow[r\to\infty]{} \frac{1}{2iq_j}\left[\delta_{1j}\frac{u_j^{(+)}(q_j r)}{r} + A_j(q)\frac{u_j^{(-)}(q_j r)}{r} \right]. \qquad (5)$$

Here $q_j = \sqrt{2\mu_j E_j}$ for open channels ($E_j \geqslant 0$) and $q_j = -i\kappa_j = -i\sqrt{2\mu_j(-E_j)}$ for closed channels ($E_j < 0$). Through these relations, all the momenta q_j can be expressed as functions of q. Also, $u_j^{(\pm)}(q_j r)$ denotes the outgoing (+) or incoming (−) asymptotic wave; it is the spherical wave $e^{\pm i q_j r}$ for channels without the Coulomb force, while the Coulomb wave function needs to be used for charged particles, $u_j^{C(\pm)}(q_j r) = \pm e^{\mp i\sigma_j}[iF(q_j r) \pm G(q_j r)]$ with $\sigma_j = \arg\Gamma(1 + i\eta_j)$, $\eta_j = -\mu_j\alpha/q_j$, and $F(x)$ [$G(x)$] being the regular [irregular] Coulomb wave function.

In the following subsections, we discuss the coupled-channels treatment with $p\Xi^-$ and $\Lambda\Lambda$ as measured channels.

B. $p\Xi^-$ correlation function

Let us consider the $p\Xi^-$ correlation function and assign the channel indices $i = 1, 2$, and 3 as $p\Xi^-$, $n\Xi^0$, and $\Lambda\Lambda$, respectively. For the $p\Xi^-$ pair, there are two s-wave channels, spin 0 (singlet) and spin 1 (triplet). The former couples to the singlet $n\Xi^0$ and $\Lambda\Lambda$ channels, while the latter couples only to the triplet $n\Xi^0$ channel. What we observe in experiments is the spin-averaged correlation function given by

$$C_{p\Xi^-}(q) = \tfrac{1}{4}C_{p\Xi^-}^{\rm singlet}(q) + \tfrac{3}{4}C_{p\Xi^-}^{\rm triplet}(q). \qquad (6)$$

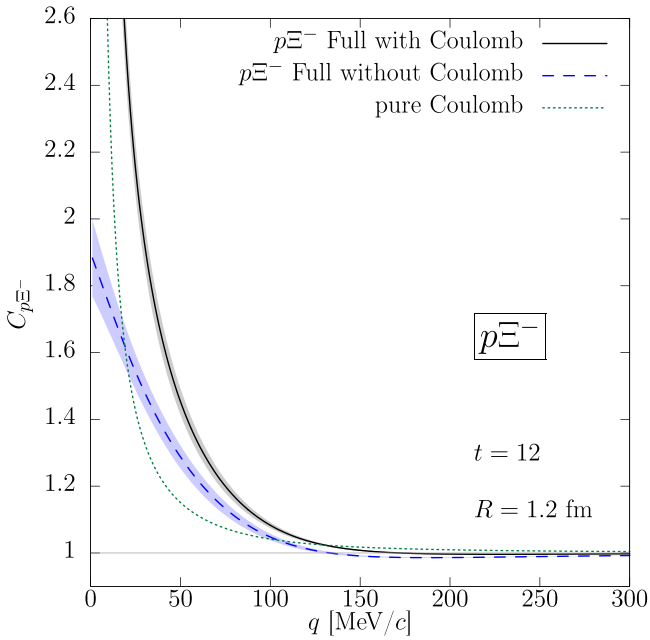

FIG. 3. The $p\Xi^-$ correlation function with the HAL QCD potential. The solid (dashed) line corresponds to the case with (without) the Coulomb interaction. The statistical error from the lattice QCD data is shown by the shaded area. The correlation function only with the Coulomb interaction is shown by the dotted line.

For $p\Xi^-$, it is necessary to treat the Coulomb interaction carefully because it distorts the wave function significantly in the small momentum region. We introduce the Coulomb potential $V_{\rm C}(r) = -\alpha/r$ to the diagonal component of the $p\Xi^-$ channel as $V^{\rm QCD}_{p\Xi^-}(r) + V_{\rm C}(r)$. Since the long-range Coulomb force affects all the partial waves while the short-range strong force affects only the s wave at low energies, the wave function in channel 1 ($p\Xi^-$) in Eq. (3) should be written as [23]

$$\Psi_1^{(-)}(\boldsymbol{q};\boldsymbol{r}) = \left(\phi^{\rm C}(\boldsymbol{q};\boldsymbol{r}) - \phi_0^{\rm C}(qr)\right) + \psi_1^{(-)}(q;r), \tag{7}$$

where $\phi^{\rm C}(\boldsymbol{q};\boldsymbol{r})$ is the free Coulomb wave function and $\phi_0^{\rm C}(qr)$ is its s-wave component. The boundary condition for $\psi_j^{(-)}(q;r)$ must be given by the the Coulomb wave function $u_j^{{\rm C}(\pm)}(q_j r)$ for $j = 1$ and the spherical wave $e^{\pm i q_j r}$ for $j = 2$ and 3 in Eq. (5). Then the KPLLL formula can be written as

$$C(q) = \int d^3r\, S_1(r)\left[\left|\phi^{\rm C}(\boldsymbol{q};\boldsymbol{r})\right|^2 - \left|\phi_0^{\rm C}(qr)\right|^2\right] + \sum_{j=1}^{3}\int_0^\infty 4\pi r^2 dr\, \omega_j S_j(r)|\psi_j^{(-)}(q;r)|^2. \tag{8}$$

In Fig. 3, we show the fully coupled-channels results of the $p\Xi^-$ correlation function with and without the Coulomb attraction (the solid line and the dashed line, respectively), together with the case of pure Coulomb attraction (the dotted line). Here we use the $N\Xi$-$\Lambda\Lambda$ coupled-channels potential at $t = 12$ given in Fig. 2. To see the qualitative behavior of $C_{p\Xi^-}(q)$, we take a common source function of Gaussian shape for all channels $S_j(r) = S_R(r)$ with $R = 1.2$ fm and $\omega_j = 1$ for all j. The error bands for the solid and dashed lines estimated by the jackknife method reflect the statistical errors of the lattice QCD data. Compared to the pure Coulomb case, the correlation function shows a large enhancement by the strong interaction in the low momentum region, $q < 100$ MeV.

To see the individual contribution in the j sum in Eq. (8), we plot in the left panel of Fig. 4 the three cases for $C_{p\Xi^-}(q)$ with the same parameters as Fig. 3: $j = 1$ ($p\Xi^-$ only), $j = 1$ and 3 ($p\Xi^- + \Lambda\Lambda$), and $j = 1, 2$, and 3 ($p\Xi^- + n\Xi^0 + \Lambda\Lambda$). For simplicity, the statistical errors are not shown. One finds that the major enhancement of $C_{p\Xi^-}(q)$ over the pure Coulomb case comes from the $N\Xi$ attraction, while the channel coupling to $\Lambda\Lambda$ is negligible. Further decomposition into spin singlet $C^{\rm singlet}_{p\Xi^-}(q)$ and spin triplet $C^{\rm triplet}_{p\Xi^-}(q)$ are shown in the middle and right panels of Fig. 4, respectively. Due to the larger negative scattering length in the spin-singlet channel, its enhancement is stronger, although the spin degeneracy factor is smaller. Also, we find that the contribution from the $n\Xi^0$ channel source to the singlet correlation function gives a small enhancement, while the $\Lambda\Lambda$ source is almost negligible. For the triplet correlation function, the contribution from the $n\Xi^0$ source is almost invisible.

C. $\Lambda\Lambda$ correlation function

To study the $\Lambda\Lambda$ correlation function, we assign the channel indices $i = 1$, 2, and 3 to $\Lambda\Lambda$, $n\Xi^0$, $p\Xi^-$, respectively. For identical particles, the wave function (3) is distorted by the quantum statistical effect. Then the wave function in channel 1 ($\Lambda\Lambda$) can be decomposed in the even parity (spin-singlet) and the odd parity (spin-triplet) components as

$$\Psi^{(-)}_{1,{\rm E}}(\boldsymbol{q};\boldsymbol{r}) = \frac{1}{\sqrt{2}}[\Psi_1^{(-)}(\boldsymbol{q};\boldsymbol{r}) + \Psi_1^{(-)}(\boldsymbol{q};-\boldsymbol{r})] \tag{9}$$

$$= \sqrt{2}[[\cos(\boldsymbol{q}\cdot\boldsymbol{r}) - \phi_0(qr)] + \psi_1^{(-)}(q;r)], \tag{10}$$

$$\Psi^{(-)}_{1,{\rm O}}(\boldsymbol{q};\boldsymbol{r}) = \frac{1}{\sqrt{2}}[\Psi_1^{(-)}(\boldsymbol{q};\boldsymbol{r}) - \Psi_1^{(-)}(\boldsymbol{q};-\boldsymbol{r})] \tag{11}$$

$$= \sqrt{2} i \sin(\boldsymbol{q}\cdot\boldsymbol{r}). \tag{12}$$

Since we consider only the s-wave distortion by the strong interaction, the scattering wave function ψ_j appears only in the even parity part. Thus the even and odd parity correlation functions are given by

$$C_{\rm E}(q) = \int d^3r \sum_{j=1}^{3}\omega_j S_j(r)|\Psi^{(-)}_{j,{\rm E}}(\boldsymbol{q};\boldsymbol{r})|^2 \tag{13}$$

$$= 1 + \exp(-4q^2R^2) + 2\int d^3r \sum_{j=1}^{3}\omega_j S_j(r)[|\psi_j^{(-)}(q;r)|^2 - |\phi_0(qr)|^2\delta_{1j}], \tag{14}$$

$$C_{\rm O}(q) = \int d^3r \sum_{j=1}^{3}\omega_j S_j(r)|\Psi^{(-)}_{j,{\rm O}}(\boldsymbol{q};\boldsymbol{r})|^2 \tag{15}$$

$$= 1 - \exp(-4q^2R^2). \tag{16}$$

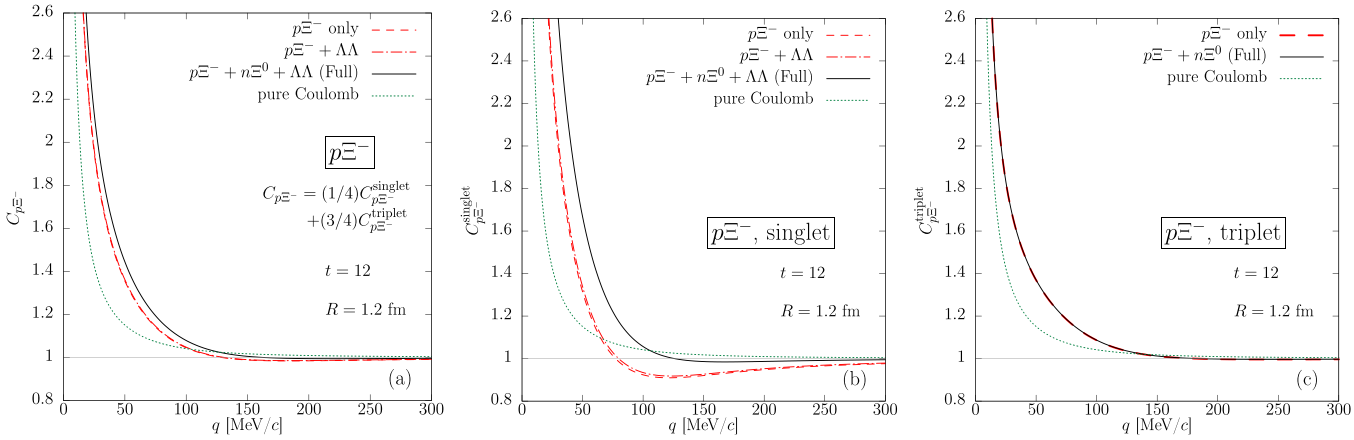

FIG. 4. The breakdown of the $p\Xi^-$ correlation function. The left panel shows the spin-averaged correlation function given by Eq. (6). The middle and right panels show the correlation function of spin single and triplet channels, respectively. The dashed lines denote the correlation function calculated only with the $p\Xi^-$ wave function. The dash-dotted line and solid line denote the results with the contributions of $p\Xi^- + \Lambda\Lambda$ and $p\Xi^- + n\Xi^0 + \Lambda\Lambda$ channels, respectively.

Taking into account the spin degrees of freedom, the final form of the $\Lambda\Lambda$ correlation function reads

$$C_{\Lambda\Lambda}(q) = \frac{1}{4}C_{\rm E}(q) + \frac{3}{4}C_{\rm O}(q) \tag{17}$$

$$= 1 - \frac{1}{2}\exp(-4q^2R^2) + \frac{1}{2}\int d^3r \sum_{j=1}^{3}\omega_j S_j(r) \times [|\psi_j^{(-)}(q;r)|^2 - |\phi_0(qr)|^2]. \tag{18}$$

The $\Lambda\Lambda$ correlation is always suppressed by $(1/2)\exp(-4q^2R^2)$ by the quantum statistical effect, which is independent of the interactions.

We note here that, if the energy is above the $p\Xi^-$ threshold ($E_3 > 0$), $p\Xi^-$ is an open channel and the asymptotic wave function is given by the Coulomb wave function as

$$\psi_3^{(-)}(q;r) \xrightarrow[r\to\infty]{} \frac{A_3(q)}{2iq_3}\frac{u_3^{{\rm C}(-)}(q_3r)}{r}. \tag{19}$$

If the energy is less than the $p\Xi^-$ threshold ($E_3 < 0$), q_3 should be replaced by $-i\kappa_3$ in the above expression, so that we have $u_3^{{\rm C}(-)}(q_3r) = e^{i\pi|\eta_3|/2}W_{|\eta_3|,1/2}(2\kappa_3 r)$ with $W_{k,\ell+1/2}(z)$ being the Whittaker function [37,38].

In Fig. 5, we show the fully coupled-channels result of the $\Lambda\Lambda$ correlation function (the solid line) together with the case of pure quantum statistics contribution (the dotted line). The coupled-channels potentials at $t = 12$ given in Fig. 2 are employed, and a common source function of Gaussian shape is assumed for all channels as in the case of Fig. 3. The error band for the solid line reflecting the statistical errors of the lattice QCD data is estimated by the jackknife method.

Compared to the case of pure quantum statistics, $C_{\Lambda\Lambda}(q)$ shows a strong enhancement by the strong interaction in the low momentum region: $q < 100$ MeV. Also, two cusps corresponding to the $n\Xi^0$ threshold at 2254 MeV and the $p\Xi^-$ threshold at 2260 MeV are found as previously pointed out in Ref. [26]. Such a threshold cusp is indeed found experimentally in the K^-p correlation function [26,28,39]. In the present case, these cusps are rather moderate due to the weak coupling between $\Lambda\Lambda$ and $N\Xi$, and it would be a challenging problem to find them experimentally.

To see the individual contribution in the j sum in Eq. (18), we plot in Fig. 6 the three cases for $C_{\Lambda\Lambda}(q)$ with the same parameters as Fig. 5: $j = 1$ ($\Lambda\Lambda$ only), $j = 1$ and 2 ($\Lambda\Lambda + n\Xi^0$), and $j = 1, 2$, and 3 ($\Lambda\Lambda + n\Xi^0 + p\Xi^-$). For simplicity, the statistical errors are not shown. The figure shows that the $n\Xi^0$ and $p\Xi^-$ sources only affect the cusp region, and make little contribution to the other momentum region. Nevertheless, solving the coupled-channels Schrödinger equation (4) is important to take into account the extra $\Lambda\Lambda$ attraction due to the coupling with $N\Xi$ states.

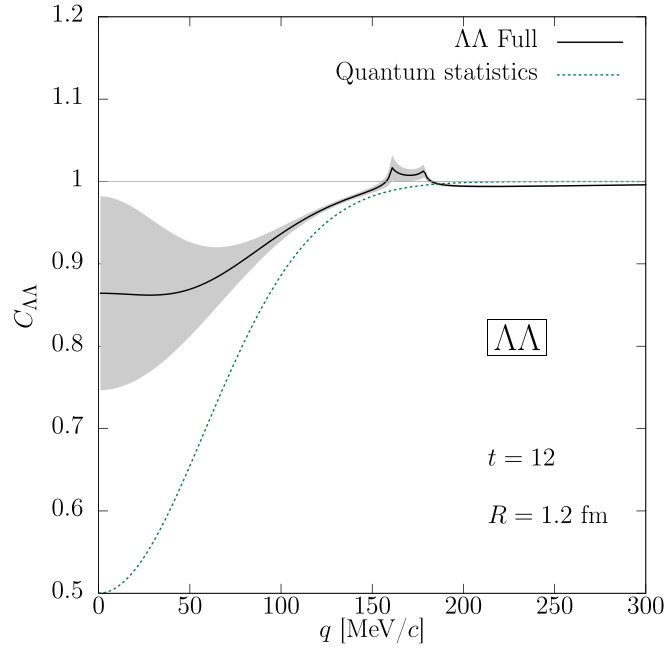

FIG. 5. The $\Lambda\Lambda$ correlation function. The statistical error of the lattice QCD data is shown by the shaded area. The result of pure quantum statistics without strong interaction is shown by dotted line.

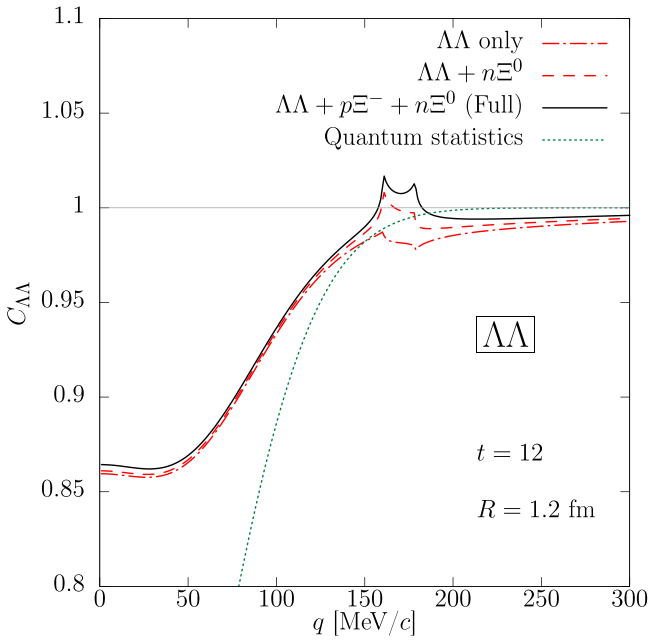

FIG. 6. The breakdown of the $\Lambda\Lambda$ correlation function. The dashed line denotes the correlation function calculated only with the $\Lambda\Lambda$ wave function component. The dash-dotted (the solid line) denote the results in which the contribution from the $n\Xi^0$ (all the coupled channels) are added. The dotted line denotes the pure quantum statics case, where all the final state interactions are switched off.

IV. DETERMINATION OF PARAMETERS

A. Source function and weight

For pp and pA collisions, a spherical and static Gaussian source function works well to reproduce the data. In the present analysis of the correlation functions in pp and pA collisions we adopt the static Gaussian source function:

$$S_j(r) = \frac{1}{\left(4\pi R_j^2\right)^{3/2}} \exp\left(-\frac{r^2}{4R_j^2}\right). \tag{20}$$

Here, the effective source size R_j would depend on hadron pairs and reactions [40]. In experiments, the source size has been studied by using the correlation function of the pp pairs for which the elaborated strong interaction potential is available. For the pp pairs, the ALICE Collaboration has previously determined R_{pp} to be $R_{pp}^{\rm ALICE}(pp) = 1.182 \pm 0.008({\rm stat})^{+0.005}_{-0.002}({\rm syst})$ fm in pp collisions at 13 TeV and $R_{pp}^{\rm ALICE}(p{\rm Pb}) = 1.427 \pm 0.007({\rm stat})^{+0.001}_{-0.014}({\rm syst})$ fm in pPb collisions at 5.02 TeV [11,16]. On the other hand, smaller source sizes are reported for $p\Xi^-$ and $p\Omega^-$ pairs: $R_{p\Xi^-}^{\rm ALICE}(pp) = 1.02 \pm 0.05$ fm and $R_{p\Omega^-}^{\rm ALICE}(pp) = 0.95 \pm 0.06$ fm [17]. In the present paper, we assume that the source sizes of $N\Xi$ pairs and $\Lambda\Lambda$ pairs are the same ($R_j = R$), since their total masses are close to each other and the contribution from the coupled-channels sources is not large.

In the theoretical analysis in Sec. III, we set $\omega_j = 1$ for simplicity. In actual high energy collisions, the source weights depend on the channel and the reaction. In general, the ratio of the source weights in channels i and j is written in terms of the particle yields N as $\frac{\omega_j}{\omega_i} = \frac{\alpha_j N(j_1)N(j_2)}{\alpha_i N(i_1)N(i_2)}$ with i_1, i_2, j_1, and j_2 being the labels of particles in each channel and α_i representing the ratio of the number of particle pairs assigned to channel i among $N(i_1) \times N(i_2)$ pairs. For the $K^- p$ correlation function analyses in Ref. [28], a statistical model [41,42] provides a reasonable estimate of the source weights. Accordingly, we evaluate the ratio in terms of thermal Boltzmann factor with the corresponding baryon mass,

$$\frac{\omega_j}{\omega_i} = \frac{\alpha_j}{\alpha_i} \exp\left[\left(m_{i_1} + m_{i_2} - m_{j_1} - m_{j_2}\right)/T_*\right], \tag{21}$$

where $T_* = 154$ MeV is the hadronization temperature [41,42][2]. The factors $\alpha_{j,i}$ are given by the spin degree and the ratio of particle pairs: $\alpha_{\Lambda\Lambda} = 1/2$ due to its identical particle nature and $\alpha_{N\Xi(J=0)} = 1/4$ ($\alpha_{N\Xi(J=1)} = 3/4$) due to its spin degeneracy.

It should be noted that the analysis of the correlation function from AA collisions requires more detailed information on the source function, e.g., asymmetrical distribution shape and flow effects [9]. Also, in small collision systems, the detailed feature of the hadronization process may contribute to the source function. In practice, it is not easy to construct a theoretical model which describes dynamical evolution of heavy-ion collisions and the femtoscopic data simultaneously [43,44]. One of the alternative ways is to rely on the systematics. For example, ALICE Collaboration proposes a common baryon source in high-multiplicity pp collisions [40], where a common core source size is given as a function of the transverse mass, the effect of strong resonance decay is taken into account, and the effective static Gaussian source size is evaluated. Then the correlation functions of several different pairs are successfully explained. Thus the details of the source are expected to be renormalized into the effective source size in the present precision of the hadron interactions with strangeness.

B. Fitting procedure

The experimental data of the correlation functions contain not only the physical effect of the final state interactions but also contaminations from the particle misidentification, the feed-down effect from weak and electromagnetic decays of other particles, and the nonfemtoscopic effect such as the minijet contribution. To take into account those effects, we adopt the following fitting function proposed by the ALICE Collaboration [10,16]:

$$C_{\rm fit}(q) = (a + bq)[1 + \lambda(C_{\rm th}(q) - 1)]. \tag{22}$$

Here the first factor in the right-hand side parametrizes non-femtoscopic backgrounds. The particle misidentification and the feed-down effect are represented by the pair purity probability λ which are estimated in Refs. [11,16] and are recapitulated in Table II. Other correlations feeding into the

[2]Equation (21) gives a slightly different relative weight $\omega_{N\Xi}/\omega_{\Lambda\Lambda}$ from the statistical model due to the approximation that holds for $m_{j_1} m_{j_2}/(m_{i_1} m_{i_2}) \sim 1$. We have checked that this factor does not change the following qualitative results and the pictures.

TABLE II. The pair purity λ, nonfemtoscopic parameters a and b, and the effective source size R in the fitting function $C_{\rm th}(q)$. The parameters a and b in pp ($\Lambda\Lambda$ pairs) and pPb ($p\Xi^-$ and $\Lambda\Lambda$ pairs) collisions and R in pp collisions are the actual fitting parameters. Numbers with references are taken from Refs. [11,16,17], and the number with $(*)$ is estimated from other other parameters. See the text for details.

Collision	Pair	λ	a	b [(MeV/c)$^{-1}$]	R (fm)
pp	$p\Xi^-$	1 [17]	1 [17]	0 [17]	1.05
(13 TeV)	$\Lambda\Lambda$	0.338 [11]	0.95	1.28×10^{-4}	
pPb	$p\Xi^-$	0.513 [16]	1.09	-2.56×10^{-4}	$1.27^{(*)}$
(5.02 TeV)	$\Lambda\Lambda$	0.239 [11]	0.99	0.29×10^{-4}	

present channels are assumed to be flat. For the theoretical two-particle correlation function $C_{\rm th}(q)$, we employ the results of the HAL QCD potential in Sec. III. We note here that the experimental data for the $p\Xi^-$ correlation function in pp collisions given in Ref. [17] are obtained after the subtraction of the nonfemtoscopic background, the particle misidentification, and the feed-down effect, so that we should take $(\lambda, a, b) = (1, 1, 0)$ as indicated in Table II.

We carry out a simultaneous fit of the ALICE data of $p\Xi^-$ and $\Lambda\Lambda$ correlations in pp collisions [11,17] by using $C_{\rm fit}(q)$ in Eq. (22). There are three fitting parameters, $a_{\Lambda\Lambda}$, $b_{\Lambda\Lambda}$, and $R(pp)$; other parameters are fixed as given in Table II. Then we found $a_{\Lambda\Lambda} = 0.95$, $b_{\Lambda\Lambda} \simeq 10^{-4}$(MeV/$c$)$^{-1}$, and $R(pp) = 1.05$ fm with χ^2/(d.o.f.) $\simeq 1$. Our source size is in good agreement with $R^{\rm ALICE}_{p\Xi^-}(pp) = 1.02 \pm 0.05$ fm [17].

For $p\Xi^-$ and $\Lambda\Lambda$ correlation functions in pA collisions [11,16], large uncertainties of the data do not allow us to determine the source size $R(p$Pb) precisely. Indeed, χ^2/(d.o.f.) depends on R only weakly and stays above 1. Thus we estimate $R(p$Pb) by combining our $R(pp)$ and the ALICE results on the system dependence of the pp pairs: $R(p\text{Pb}) = R(pp) \times R^{\rm ALICE}_{pp}(p\text{Pb})/R^{\rm ALICE}_{pp}(pp) = 1.27$ fm. [3] After fixing $R(p$Pb) in this way, we carry out a simultaneous fit of the ALICE data of the $p\Xi^-$ and $\Lambda\Lambda$ correlation functions in pPb collisions with the four fitting parameters $a_{\Lambda\Lambda}$, $b_{\Lambda\Lambda}$, $a_{p\Xi^-}$, and $b_{p\Xi^-}$ to obtain the values in Table II.

Some remarks about the fitting procedure are in order here. (i) The statistical and systematic errors of the experimental data are added in quadrature in our fit. (ii) We use the data up to $q = 300$ MeV/c for the $p\Xi^-$ pairs in pp collisions, while the data up to $q = 500$ MeV/c are used in other cases. This is because the nonfemtoscopic backgrounds are subtracted in the former case, while we need high-momentum data to determine a and b in the latter case. (iii) We take the HAL QCD potential with $t = 12$ to carry out the fit $C_{\rm th}$. Uncertainties arising from this statistical and systematic errors of the HAL QCD potential are also considered in the final results.

[3] We note that we have realized that the event types are different among the correlation functions analyzed here. The correlation function of $p\Xi^-$ from pp collisions [17] is obtained from the high-multiplicity events, while other correlation functions (the $\Lambda\Lambda$ [11] correlation function from pp collisions and the $p\Xi^-$ [16] and $\Lambda\Lambda$ [11] correlation functions from pPb collisions) are from minimum bias events. Since the source size generally increases with increasing multiplicity, the present source size, $R(pp)$ for $\Lambda\Lambda$ and $R(p$Pb) for $p\Xi^-$ and $\Lambda\Lambda$, may overestimate the realistic ones. This is consistent with the fact that the χ^2 is smaller with a smaller source size for pPb collisions. It should be noted, however, that χ^2/(d.o.f.) values are not very different and then the correlation functions shown below look similar to those with a little smaller source size, and thus we use the above explained source size.

V. COMPARISON WITH EXPERIMENTAL DATA

A. $p\Xi^-$ correlation function

In the upper panels of Fig. 7, our final results of the $p\Xi^-$ correlation functions are compared with the $p\Xi^-$ data in pp collisions at 13 TeV (the left panel) and in pPb collisions at 5.02 TeV (the right panel) [16,17]. The solid lines denote our final results with statistical and systematic errors of the HAL QCD potential. The former is estimated by the jackknife method with the $t = 12$ data, and the latter is estimated by the potentials for $t = 11$ and 13. The dotted green lines are the results with the Coulomb potential only. Shown by the shaded region is the larger one among the statistical and systematic errors.

The solid lines explain not only the strong enhancement at small q but also the q dependence of $C_{p\Xi^-}(q)$. The enhancement over the pure Coulomb potential implies the attractive nature of the strong $N\Xi$ interaction. Such an observation has been already reported in the previous works [16,17,24,26]. However, our paper provides for the first time the coupled-channels analysis with the threshold difference, the strong interaction, and the Coulomb interaction taken into account. (Neither the coupled-channels effect nor the threshold difference was considered in Refs. [16,17,24], while the Coulomb interaction was not considered in Ref. [26].) We note that the agreement of the correlation function in Refs. [16,17] and that in the present work comes from the fact that the coupled-channels effects are not significant in the $p\Xi^-$ correlation function due to weak transition between $p\Xi^-$ and $\Lambda\Lambda$.

B. $\Lambda\Lambda$ correlation function

In the lower panels of Fig. 7, our final results of the $\Lambda\Lambda$ correlation functions are compared with the $\Lambda\Lambda$ data in pp collisions at 13 TeV (the left panel) and in pPb collisions at 5.02 TeV (the right panel) [11]. The solid lines denote our final results with statistical and systematic errors of the HAL QCD potential. The dotted green lines are the results with only the quantum statistics effect. Although there are large uncertainties of the experimental data at small q region, the agreement of the solid line with the data indicates a weak attraction in the $\Lambda\Lambda$ channel without a deep bound state. This is consistent with the conclusions in Refs. [10,11].

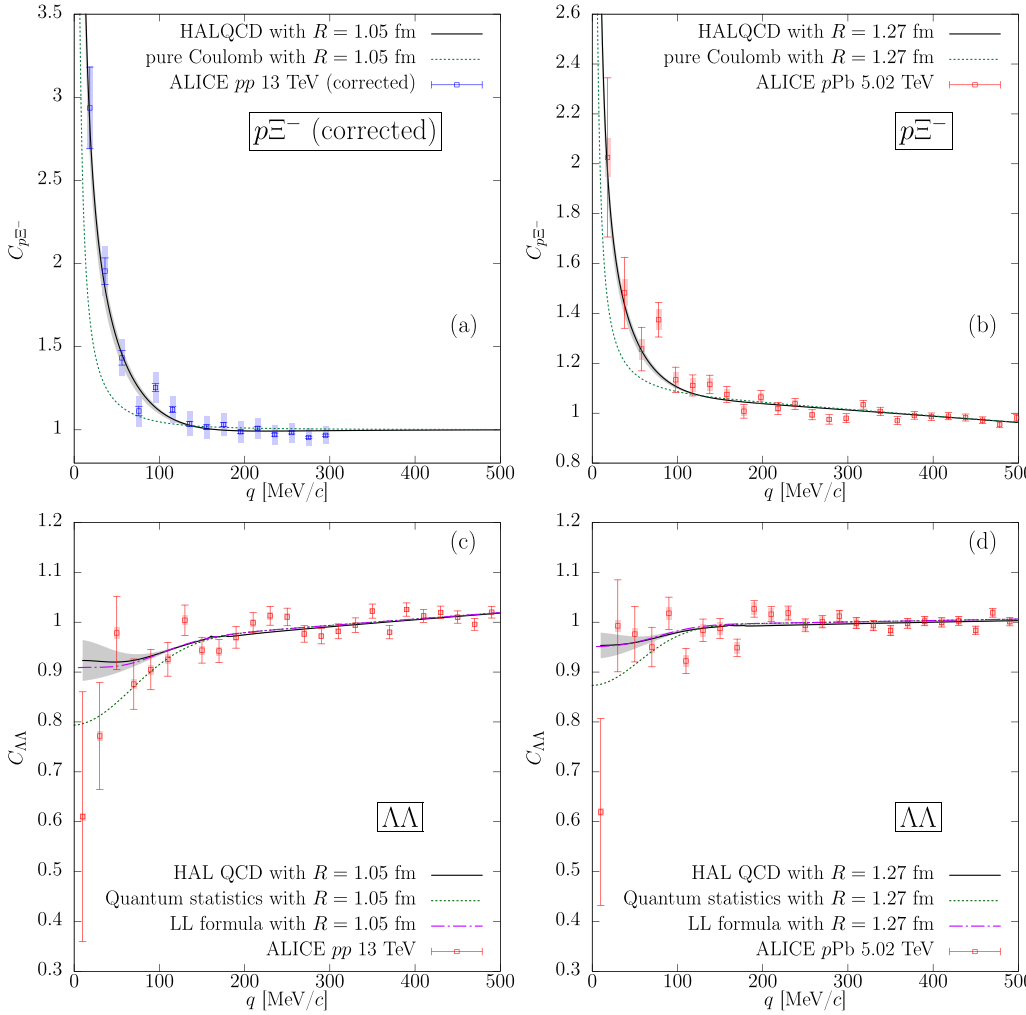

FIG. 7. Experimental and theoretical correlation functions of the $p\Xi^-$ pairs (the upper panels) and the $\Lambda\Lambda$ pairs (the lower panels). The blank squares are the ALICE data taken from Refs. [11,16,17]; the statistical error and systematic error are denoted by the vertical line and the shaded bar, respectively. Solid lines are the theoretical results with statistical and systematic uncertainties represented by the shaded region. The left (right) panels correspond to the results in pp collisions at 13 TeV (pPb collisions ar 5.02 TeV). The dotted lines show the results with only Coulomb interaction (only quantum statistics) for the $p\Xi^-$ ($\Lambda\Lambda$) correlation functions. The dash-dotted lines show the correlation function calculated with the LL formula.

The correlation functions calculated with the Lednicky-Lyuboshits (LL) formula for identical spin-half baryon pairs [33] are also plotted in the lower panels of Fig. 7 by the dash-dotted line:

$$C(q) = 1 - \frac{1}{2}\, e^{-4q^2R^2} + \frac{1}{2}\Delta C(q), \tag{23}$$

$$\Delta C(q) = \frac{|f(q)|^2}{2R^2} F_3\left(\frac{r_{\rm eff}}{R}\right) + \frac{2{\rm Re}f(q)}{\sqrt{\pi}R} F_1(2qR) - \frac{{\rm Im}f(q)}{R} F_2(2qR), \tag{24}$$

where $F_1(x) = \int_0^x dt\, e^{t^2-x^2}/x$, $F_2(x) = (1 - e^{-x^2})/x$, $F_3(x) = 1 - x/2\sqrt{\pi}$, and we make the effective range expansion of single channel $\Lambda\Lambda$ scattering amplitude $f(q)$ with $a_0 = -0.78$ fm and $r_{\rm eff} = 5.4$ fm given in Table I. The same non-femtoscopic parameters and the pair purity listed in Table II are used. We find that the single-channel LL formula gives a good approximation to the fully coupled-channels results for a wide range of q in both pp and pPb collisions. It would be interesting to see whether high precision data for $C_{\Lambda\Lambda}(q)$ in the future may reveal cusp structures at the $n\Xi^0$ and $p\Xi^-$ thresholds as expected from the coupled-channels effect.

C. System size dependence

The enhancement of $C(q)$ for fixed R alone cannot conclude whether a bound or quasibound state is generated by the strong interaction. This can be demonstrated by using an analytic model for neutral and nonidentical particles $C(q) = 1 + \Delta C(q)$ with $r_{\rm eff} = 0$, which is obtained from Eq. (24) as

$$\Delta C(q) = \frac{1}{x^2 + y^2}\left[\frac{1}{2} - \frac{2y}{\sqrt{\pi}} F_1(2x) - xF_2(2x)\right], \tag{25}$$

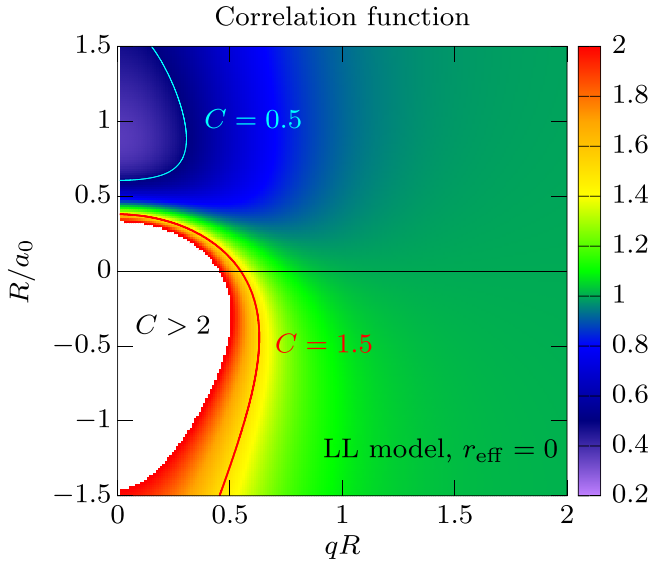

FIG. 8. The contour plot of the correlation function $C(q)$ in the LL analytic model at $r_{\rm eff} = 0$ as a function of $x = qR$ and $y = R/a_0$.

with $x = qR$ and $y = R/a_0$. Shown in Fig. 8 is a contour plot of $C(q)$ in the x-y plane. The strongly enhanced region $C(q) > 2$ indicated by the white area extends to both negative and positive sides of y for $x < 0.5$. (Even if one introduces the Coulomb attraction as in the case of $p\Xi^-$, this situation does not change qualitatively, as discussed in Appendix C.)

Scanning through the y axis by changing the system size R would provide further experimental information on the sign of y. To demonstrate this, we show the $p\Xi^-$ and $\Lambda\Lambda$ correlation functions for several different source sizes ($R = 0.9,\ 1.2,\ 1.5$, and 3 fm) in Fig. 9 with the HAL QCD potential (the thick lines) and without the HAL QCD potential (the thin lines).

For the $p\Xi^-$ correlation function, Fig. 9 implies that the enhancement of $C(q)$ due to strong interaction over the pure Coulomb attraction is significant around $R = 1$ fm but is gradually reduced toward the larger values of R. This is consistent with the fact that we are in the negative y region as indicated by Fig. 8. If the scattering length is in the bound region ($y = R/a_0 > 0$), we would expect that $C(q)$ undershoots the Coulomb contribution and may form a dip as a function of $x = qR$. Thus the experimental studies of the $p\Xi^-$ correlation function in heavy-ion collisions corresponding to larger R are of particular interest.

For the $\Lambda\Lambda$ correlation function, Fig. 9 shows that the enhancement of $C(q)$ due to strong interaction over the pure quantum statistics has characteristic nonmonotonic behavior for q smaller than the $N\Xi$ threshold. However, to have quantitative discussions for large R corresponding to the heavy-ion collisions, more realistic source shape as well as the flow effect need to be taken into account [9], since the effect of quantum statistics is particularly important in the $\Lambda\Lambda$ correlation.

We note here that a high-momentum tail of the $\Lambda\Lambda$ correlation function above the $N\Xi$ threshold was observed in Au + Au collisions at the Relativistic Heavy Ion Collider (RHIC) [45], and a residual source having a small size ($R_{\rm res} \simeq$ 0.5 fm) was introduced in previous works [9,22,45]. Although it was suggested in Ref. [46] that the coupled-channels effects may explain the high-momentum tail in Au + Au collisions, the present analysis shows that such a tail does not appear unless R is smaller than 1 fm, as shown in Fig. 9. Thus this issue is still left open for future studies.

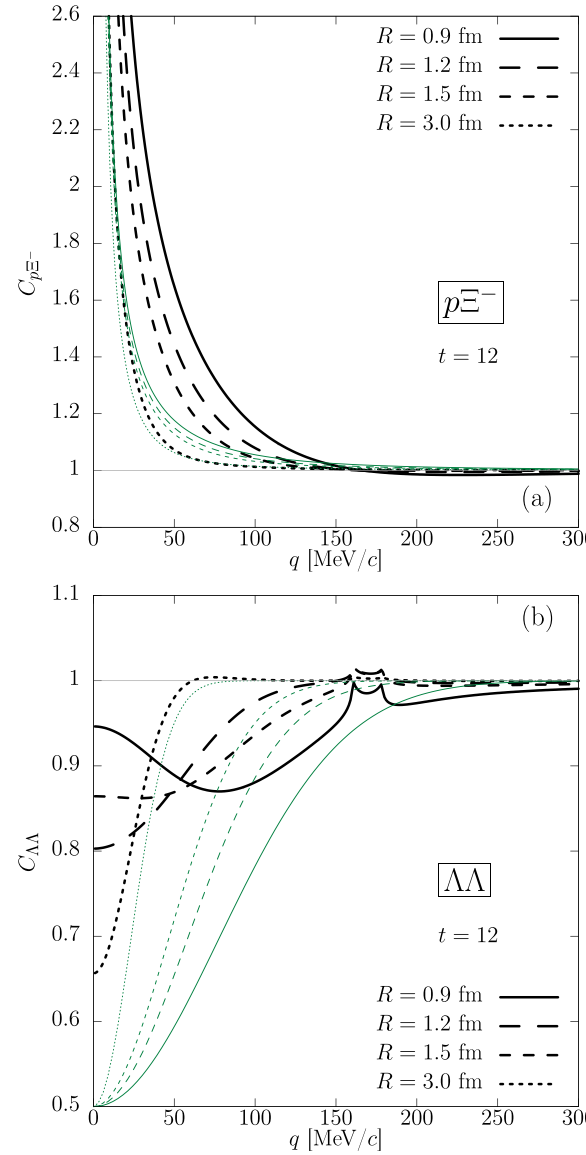

FIG. 9. Source size dependence of the $p\Xi^-$ and $\Lambda\Lambda$ correlation functions. The thick lines denote the results with full coupled-channels calculation. For comparison, the calculations with the pure Coulomb cases (pure quantum statics cases) are shown for $p\Xi^-$ ($\Lambda\Lambda$) correlation function by thin lines.

VI. SUMMARY

We studied the $p\Xi^-$ and $\Lambda\Lambda$ femtoscopy in pp and pPb collisions at LHC by using the latest $N\Xi$-$\Lambda\Lambda$ coupled-channels HAL QCD potential. A moderate $N\Xi$ attraction of this potential produces a virtual pole below the $n\Xi^0$ threshold. On the basis of the KPLLL formula for the momentum cor-

TABLE III. Same with Table I but with the pion and kaon masses in the fitted HAL QCD potential in Ref. [12] by the isospin averaged physical masses, $m_\pi = 137.3$ MeV and $m_K = 495.6$ MeV.

Total spin	Baryon pair	a_0 (fm)	$r_{\rm eff}$ (fm)
$J = 0$	$p\Xi^-$	$-1.25(0.03)(^{+0.12}_{-0.00}) - i2.00(0.40)(^{+0.16}_{-0.31})$	$3.7(0.3)(^{+0.0}_{-0.1}) - i2.4(0.2)(^{+0.1}_{-0.3})$
	$n\Xi^0$	$-2.76(0.63)(^{+0.33}_{-0.66}) - i0.15(0.12)(^{+0.00}_{-0.03})$	$1.5(0.3)(^{+0.0}_{-0.1}) - i0.1(0.0)(^{+0.0}_{-0.0})$
	$\Lambda\Lambda$	$-0.99(0.30)(^{+0.00}_{-0.17})$	$4.9(0.70)(^{+0.1}_{-0.5})$
$J = 1$	$p\Xi^-$	$-0.47(0.08)(^{+0.11}_{-0.09}) - i0.0(0.00)(^{+0.00}_{-0.00})$	$6.7(0.7)(^{+1.4}_{-0.9}) + i0.0(0.1)(^{+0.0}_{-0.0})$
	$n\Xi^0$	$-0.47(0.08)(^{+0.11}_{-0.09})$	$6.8(0.7)(^{+1.4}_{-0.9})$

relations of hadron pairs, we considered the coupled-channels effect, the threshold difference, the strong interaction, and the Coulomb interaction at the same time to analyze the $p\Xi^-$ and $\Lambda\Lambda$ correlation functions. After evaluating the parameters of the nonfemtoscopic effects and the source function, theoretical results of the correlation functions are compared with the experimental data by the ALICE Collaboration; they are found to be in good quantitative agreement. From this comparison, we concluded that negative scattering lengths in the $N\Xi$ system are implied by the strong enhancement of the $p\Xi^-$ correlation function over the Coulomb contribution. Also, we found that the $\Lambda\Lambda$ correlation function may show a twin cusp near the $n\Xi^0$ and $p\Xi^-$ thresholds due to channel coupling, which would be interesting see in future high precision data.

Studies with femtoscopic techniques in different collision systems will help us to unravel the physics of hadron-hadron interactions further. For example, it is interesting to examine the $N\Xi$ correlation function in nucleus-nucleus collisions by changing the impact parameter, so that one can utilize the idea of the "small-to-large ratio" to extract the strong interaction effect without much contamination from the Coulomb interaction [23]. A femtoscopic study of the hadron-deuteron correlation functions [47–50] is another feasible and valuable direction to pursue. The production of the $S = -2$ system through the (K^-, K^+) reaction with nuclear target is also an alternative and promising approach to study the $N\Xi$-$\Lambda\Lambda$ system in a controlled fashion [51–53].

ACKNOWLEDGMENTS

The authors thank members of HAL QCD Collaboration for providing lattice QCD results of coupled-channels $N\Xi$-$\Lambda\Lambda$ interactions and for valuable discussions. The authors also thank Laura Fabbietti, Otón Vázquez Doce, Valentina Mantovani Sarti, and members of ALICE Collaboration for providing experimental data of correlation functions and for the useful discussions. This work has been supported in part by the Grants-in-Aid for Scientific Research from JSPS (Grants No. JP21H00121, No. JP21H00125, No. JP19H05150, No. JP19H05151, No. JP19H01898, No. JP19K03879, No. JP18H05236, No. JP18H05236, No. JP18H05407, No. JP16H03995, and No. JP16K17694), by the Yukawa International Program for Quark-hadron Sciences (YIPQS), by a priority issue (Elucidation of the fundamental laws and evolution of the universe) to be tackled by using Post "K" Computer, by "Program for Promoting Researches on the Supercomputer Fugaku" (Simulation for basic science: from fundamental laws of particles to creation of nuclei), by the Joint Institute for Computational Fundamental Science (JICFuS), by the National Natural Science Foundation of China (NSFC) under Grants No. 11835015 and No. 12047503, by the NSFC and the Deutsche Forschungsgemeinschaft (DFG, German Research Foundation) through the funds provided to the Sino-German Collaborative Research Center TRR110 "Symmetries and the Emergence of Structure in QCD" (NSFC Grant No. 12070131001, DFG Project-ID 196253076), by the Chinese Academy of Sciences (CAS) under Grants No. XDB34030000 and No. QYZDB-SSW-SYS013, by the CAS President's International Fellowship Initiative (PIFI) under Grant No. 2020PM0020, and by China Postdoctoral Science Foundation under Grant No. 2020M680687.

APPENDIX A: LOW ENERGY CONSTANTS FROM MODIFIED HAL QCD POTENTIAL

The HAL QCD potential used in the text is constructed at $m_\pi \simeq 146$ MeV and $m_K \simeq 525$ MeV which are slightly away from the physical point [12]. To estimate the effect of this discrepancy, we replace m_π and m_K in the parametrization of the HAL QCD potential by the isospin-averaged physical masses, 137.3 and 495.6 MeV, respectively. Resulting scattering lengths and effective ranges are shown in Table III. The numbers are consistent with those given in Table I within the errors, although the central values of the scattering length a_0 are slightly larger due to slight increase of the attraction by the smaller pion and kaon masses.

APPENDIX B: VIRTUAL POLE AND $N\Xi$ INTERACTION

Here we summarize the relation between the two-body interaction and the behavior of the pole of the scattering amplitude in the s wave, and discuss the pole near the $n\Xi^0$ threshold in the HAL QCD potential. The eigenmomentum q of the generalized eigenstate of the Hamiltonian is expressed by the pole of the scattering amplitude [54]. In the single-channel problem with a sufficiently attractive s-wave interaction, a bound state pole lies on the imaginary momentum q axis in the upper half of the complex q plane. This pole goes down along the imaginary q axis to the lower half-plane with decreasing attraction [55,56]. The pole in the lower half-plane (the virtual pole) represents the virtual state, which is not interpreted as a physical state because its wave function is not normalized in the usual sense [54]. In the complex energy $E = q^2/2\mu$ plane, both the bound and virtual poles are mapped onto the negative real axis, but they are distinguished

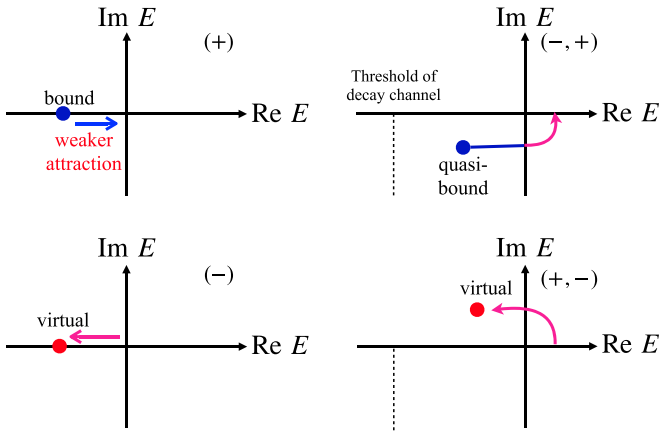

FIG. 10. A schematic picture of the s-wave pole position generated by the strong interaction in the complex energy plane. The upper left (bottom left) figure shows the pole in the (+) [(−)] sheet of the single channel case and the upper right [bottom right] right figure shows that in the (−, +) [(+, −)] sheet of the coupled-channels case (see the text for the notation of the Riemann sheets). Energy region where the pole corresponds to physical eigenstate is denoted by the blue lines. As the attractive interaction becomes weaker from the bound (quasibound) region, the bound (quasibound) pole becomes the virtual pole.

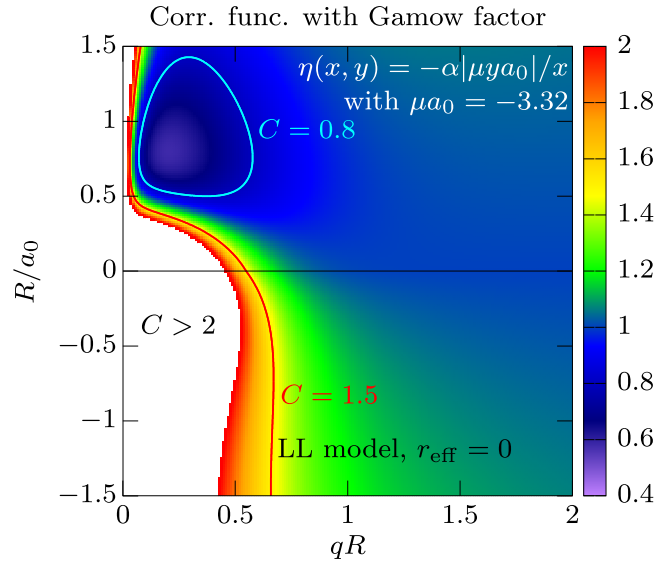

FIG. 11. Same as Fig 8 but with Gamow factor. For given $(x, y) = (qR, R/a_0)$, $\eta = -\mu\alpha/q$ is calculated as $\eta(x, y) = -\alpha|\mu y a_0|/x$ where we adopt $\mu a_0 = \mu_{p\Xi^-} a_0^{N\Xi(J=0)} = -3.32$.

by the first (+) and second (−) Riemann sheets, corresponding respectively to the Im $q > 0$ and Im $q < 0$ regions. In the complex energy plane, the bound state pole moves toward the threshold by decreasing the attraction, crosses the branch cut on Re $E > 0$ to go to the second Riemann sheet, and then becomes a virtual state moving away from the threshold (Fig. 10).

When there are decay channels at lower energy, the relation between the interaction and the pole position is modified from the single-channel case. First, with the coupling to the decay channel, the eigenenergy of the bound state is shifted to the complex energy plane, where the imaginary part represents the half decay width. Such an unstable state is called the quasibound state (would-be bound state in the absence of the decay channel). In addition, to specify the sign of the imaginary part of the eigenmomentum for each channel, the complex energy plane is defined on the 2^n-sheeted Riemann surface in the n-coupled-channels system [54]. In the simplest two-channel system, the Riemann sheet is specified by the notation $(\pm, \pm)$, representing the sign of the imaginary part of the eigenmomentum of each channel. The quasibound state should lie in the most adjacent Riemann sheet to the physical (+, +) sheet with negative imaginary part, which is the (−, +) sheet in the energy region between two thresholds. By decreasing the attraction of the potential of the higher energy channel, the pole moves toward the higher energy threshold, turns around the branch point at the threshold, and moves to the (+, −) sheet with the positive imaginary part (Fig. 10). Thus, we can find a similar behavior for a pole lying near the threshold energy.

As indicated by the negative real part of the $\Lambda\Lambda$, $n\Xi^0$ and $p\Xi^-$ scattering lengths in Table I in the case of HAL QCD potential, the strong interaction does not generate bound or quasibound states near the $\Lambda\Lambda$, $n\Xi^0$, and $p\Xi^-$ thresholds. Instead, by solving the Schrödinger equation, we find a virtual pole lying at $E_{\rm pole} = 2250.5 \pm i0.3$ MeV in the (+, −, +) sheet (in the order of $\Lambda\Lambda$, $n\Xi^0$, and $p\Xi^-$) in the $J = 0$ channel: The real part of $E_{\rm pole}$ is just below the $n\Xi^0$ threshold by −3.93 MeV. For the $N\Xi$ quasibound state to emerge, the corresponding pole should appear below the $n\Xi^0$ threshold in the (−, +, +) sheet. The near-threshold virtual pole in the (+, −, +) sheet still contributes to the enhancement of the scattering length in the $n\Xi^0$ channel. We note here that, if we use the modified HAL QCD potential associated with Table III, the virtual pole moves closer to the threshold energy of $n\Xi^0$, $E_{\rm pole} = 2251.8 \pm i0.2$ MeV. This is due to the fact that the attraction becomes slightly stronger in this case and the virtual pole moves toward the $n\Xi^0$ threshold in the complex E plane, as seen from Fig. 10.

APPENDIX C: LL MODEL WITH GAMOW FACTOR

When the Coulomb attraction operates on top of the strong interaction, $C(q)$ is enhanced in the low q region and the suppression found in Fig. 8 with $a_0 > 0$ (without the Coulomb potential) is expected to appear as a dip of $C(q)$ when the source size R is comparable to a_0. This is illustrated in Fig. 11 where the Coulomb effect is considered qualitatively by multiplying the Gamow factor given as $A_{\rm Gamow}(\eta) = 2\pi\eta/[\exp(2\pi\eta) - 1]$. On the other hand, in the negative a_0 region without the bound state, the dip structure is not expected in $C(q)$ for wide range of $R = 1$–5 fm. Recent preliminary data from Au + Au collisions [57] seem to show no dip in the $p\Xi^-$ correlation function, which is consistent with the HAL QCD potential where there is no quasibound state of $p\Xi^-$ generated by the strong interaction.

[1] M. Oka, Phys. Rev. D **38**, 298 (1988).
[2] A. Gal, Acta Phys. Pol. B **47**, 471 (2016).
[3] H. Clement, Prog. Part. Nucl. Phys. **93**, 195 (2017).
[4] R. L. Jaffe, Phys. Rev. Lett. **38**, 195 (1977); **38**, 617(E) (1977).
[5] H. Takahashi *et al.*, Phys. Rev. Lett. **87**, 212502 (2001).
[6] K. Nakazawa and H. Takahashi, Prog. Theor. Phys. Suppl. **185**, 335 (2010).
[7] S. Nishizaki, T. Takatsuka, and Y. Yamamoto, Prog. Theor. Phys. **108**, 703 (2002)-718
[8] J. M. Lattimer, Annu. Rev. Nucl. Part. Sci. **71**, 433 (2021).
[9] K. Morita, T. Furumoto, and A. Ohnishi, Phys. Rev. C **91**, 024916 (2015).
[10] S. Acharya *et al.* (ALICE Collaboration), Phys. Rev. C **99**, 024001 (2019).
[11] S. Acharya *et al.* (ALICE Collaboration), Phys. Lett. B **797**, 134822 (2019).
[12] K. Sasaki *et al.* (HAL QCD Collaboration), Nucl. Phys. A **998**, 121737 (2020).
[13] K. Nakazawa *et al.*, Prog. Theor. Exp. Phys. (2015) 033D02.
[14] S. H. Hayakawa *et al.* (J-PARC E07 Collaboration), Phys. Rev. Lett. **126**, 062501 (2021).
[15] M. Yoshimoto *et al.* (J-PARC E07 Collaboration), Prog. Theor. Exp. Phys. **2021**, 073.
[16] S. Acharya *et al.* (ALICE Collaboration), Phys. Rev. Lett. **123**, 112002 (2019).
[17] S. Acharya *et al.* (ALICE Collaboration), Nature (London) **588**, 232 (2020).
[18] J. Haidenbauer, U. G. Meißner, and S. Petschauer, Nucl. Phys. A **954**, 273 (2016).
[19] K. W. Li, T. Hyodo, and L. S. Geng, Phys. Rev. C **98**, 065203 (2018)
[20] S. Petschauer, J. Haidenbauer, N. Kaiser, Ulf-G. Meissner, and W. Weise, Front. Phys. **8**, 146 (2020).
[21] S. Aoki and T. Doi, Front. Phys. **8**, 307 (2020).
[22] A. Ohnishi, K. Morita, K. Miyahara, and T. Hyodo, Nucl. Phys. A **954**, 294 (2016).
[23] K. Morita, A. Ohnishi, F. Etminan, and T. Hatsuda, Phys. Rev. C **94**, 031901(R) (2016); **100**, 069902(E) (2019).
[24] T. Hatsuda, K. Morita, A. Ohnishi, and K. Sasaki, Nucl. Phys. A **967**, 856 (2017).
[25] D. L. Mihaylov, V. Mantovani Sarti, O. W. Arnold, L. Fabbietti, B. Hohlweger, and A. M. Mathis, Eur. Phys. J. C **78**, 394 (2018).
[26] J. Haidenbauer, Nucl. Phys. A **981**, 1 (2019).
[27] K. Morita, S. Gongyo, T. Hatsuda, T. Hyodo, Y. Kamiya, and A. Ohnishi, Phys. Rev. C **101**, 015201 (2020).
[28] Y. Kamiya, T. Hyodo, K. Morita, A. Ohnishi, and W. Weise, Phys. Rev. Lett. **124**, 132501 (2020).
[29] L. Fabbietti, V. M. Sarti, and O. Vazquez Doce, Ann. Rev. Nucl. Part. Sci. **71**, 377 (2021).
[30] S. E. Koonin, Phys. Lett. B **70**, 43 (1977).
[31] S. Pratt, Phys. Rev. D **33**, 1314 (1986).
[32] D. Anchishkin, U. W. Heinz, and P. Renk, Phys. Rev. C **57**, 1428 (1998).
[33] R. Lednicky and V. L. Lyuboshits, Yad. Fiz. **35**, 1316 (1981) [Sov. J. Nucl. Phys. **35**, 770 (1982)].
[34] R. Lednicky, V. V. Lyuboshits, and V. L. Lyuboshits, Phys. At. Nucl. **61**, 2950 (1998).
[35] N. Ishii, S. Aoki, and T. Hatsuda, Phys. Rev. Lett. **99**, 022001 (2007).
[36] N. Ishii *et al.* (HAL QCD Collaboration), Phys. Lett. B **712**, 437 (2012).
[37] M. J. Seaton, Comput. Phys. Commun. **146**, 225 (2002).
[38] C. Noble, Comput. Phys. Commun. **159**, 55 (2004).
[39] S. Acharya *et al.* (ALICE Collaboration), Phys. Rev. Lett. **124**, 092301 (2020).
[40] S. Acharya *et al.* (ALICE Collaboration), Phys. Lett. B **811**, 135849 (2020).
[41] S. Borsanyi *et al.*, Phys. Lett. B **730**, 99 (2014).
[42] A. Bazavov, T. Bhattacharya, C. DeTar, H. T. Ding, S. Gottlieb, R. Gupta, P. Hegde, U. M. Heller, F. Karsch, E. Laermann, L. Levkova, S. Mukherjee, P. Petreczky, C. Schmidt, C. Schroeder, R. A. Soltz, W. Soeldner, R. Sugar, M. Wagner, and P. Vranas, (HotQCD Collaboration), Phys. Rev. D **90**, 094503 (2014).
[43] M. A. Lisa, S. Pratt, R. Soltz, and U. Wiedermann, Annu. Rev. Nucl. Part. Sci. **55**, 357 (2005).
[44] S. Pratt, Phys. Rev. Lett. **102**, 232301 (2009).
[45] L. Adamczyk *et al.* (STAR Collaboration), Phys. Rev. Lett. **114**, 022301 (2015).
[46] A. Ohnishi, Y. Kamiya, K. Sasaki, T. Fukui, T. Hatsuda, T. Hyodo, K. Morita, and K. Ogata, Few Body Syst. **62**, 42 (2021).
[47] S. Mrówczyński and P. Słoń, Acta Phys. Pol. B **51**, 1739 (2020).
[48] F. Etminan and M. M. Firoozabadi, arXiv:1908.11484.
[49] J. Haidenbauer, Phys. Rev. C **102**, 034001 (2020).
[50] K. Ogata, T. Fukui, Y. Kamiya, and A. Ohnishi, Phys. Rev. C **103**, 065205 (2021).
[51] J. Ahn *et al.* (KEK-PS E224 Collaboration), Phys. Lett. B **444**, 267 (1998).
[52] C. J. Yoon, H. Akikawa, K. Aoki, Y. Fukao, H. Funahashi, M. Hayata, K. Imai, K. Miwa, H. Okada, N. Saito, H. D. Sato, K. Shoji, H. Takahashi, K. Taketani, J. Asai, M. Kurosawa, M. Ieiri, T. Hayakawa, T. Kishimoto, A. Sato, Y. Shimizu, K. Yamamoto, T. Yoshida, T. Hibi, K. Nakazawa, J. K. Ahn, B. H. Choi, S. J. Kim, S. H. Kim, B. D. Park, I. G. Park, J. S. Song, C. S. Yoon, K. Tanida, and A. Ohnishi (KEK-PS E522 Collaboration), Phys. Rev. C **75**, 022201(R) (2007).
[53] J. K. Ahn (J-PARC E42 Collaboration), J. Phys. Soc. Jpn. Conf. Proc. **17**, 031004 (2017).
[54] J. R. Taylor, *Scattering Theory: The Quantum Theory on Non-relativistic Collisions* (Wiley, New York, 1972).
[55] H. Masui, S. Aoyama, T. Myo, K. Katō, and K. Ikeda, Nucl. Phys. A **673**, 207 (2000).
[56] T. Hyodo, Phys. Rev. C **90**, 055208 (2014).
[57] K. Mi *et al.* (STAR Collaboration), talk at APS April Meeting 2021, L13.00007 (unpublished).